International Communications in Heat and Mass Transfer 173 (2026) 110850

Contents lists available at ScienceDirect

International Communications in Heat and Mass Transfer

journal homepage: www.elsevier.com/locate/ichmt

Thermal management in polymer sheet extrusion using physics informed neural networks and non-Fourier viscoelastic modeling

Syed Hamza Hasnain Kazmi [a,*], Noor Muhammad [b], Taha Aziz [b,c], Haitham M.S. Bahaidarah [b,d]

[a] *Abdus Salam School of Mathematical Sciences, Government College University Lahore, Pakistan*
[b] *Interdisciplinary Research Center for Sustainable Energy Systems (IRC-SES), KFUPM, Dhahran 31261, Saudi Arabia*
[c] *Department of Mathematical Sciences, DCC-KFUPM, King Fahd University of Petroleum and Minerals (KFUPM), Dhahran 31261, Saudi Arabia*
[d] *Department of Mechanical Engineering, King Fahd University of Petroleum and Minerals, Dhahran 31261, Saudi Arabia*

ARTICLE INFO

Keywords:
Physics informed neural networks
Polymer sheet extrusion
Non-Fourier heat conduction
Third grade viscoelastic flow
Cattaneo–Christov heat flux
Magnetohydrodynamics
Reactive transport
Thermal management

ABSTRACT

Efficient thermal management in polymer sheet extrusion is essential for preserving material integrity and ensuring uniform product quality. This study examines steady boundary layer flow of a third grade viscoelastic polymer melt over a stretching surface incorporating magnetohydrodynamic, porous resistance, thermal stratification, and a first order chemical reaction. Finite speed heat conduction is modeled through the Cattaneo–Christov framework to account for thermal relaxation, which is relevant in high-rate polymer processing. Benchmark solutions are first obtained using MATLAB `bvp4c` solver. A Physics Informed Neural Network is then developed in `PyTorch`, which embeds the transport equations and boundary conditions into a unified loss structure optimized through Adam and LBFGS. The neural network shows excellent consistency with the benchmark results, capturing the nonlinear interactions inherent in viscoelastic, magnetically influenced, and thermally stratified flows. The analysis demonstrates that viscoelasticity promotes momentum transport, magnetic and porous resistances suppress flow development, thermal relaxation results in the reduction of near wall heating, and chemical reaction reduces concentration levels. The combined numerical and data driven framework provides a flexible tool for predictive thermal control in polymer extrusion, coating, and related manufacturing processes.

0. Introduction

Polymer sheet extrusion and coating operations depend critically on controlled thermal conditions to maintain material integrity and reliability [1–3]. During continuous stretching, the resulting boundary layer motion involving polymer melts exhibits nonlinear viscoelastic behavior [4,5]. Classical Newtonian models are insufficient to effectively represent these processes [6]. Among differential type models, the third grade viscoelastic framework provides an effective representation of shear dependent and elastic effects, which are of typical relevance to industrial polymeric materials [7]. The stretching sheet formulation serves as a widely adopted model for the investigation of extrusion and coating technologies [8].

Conventional heat transfer analyses often rely on Fourier's law, which assumes an instantaneous response of thermal disturbances [9–11]. This assumption becomes limiting in high rate or microscale processes, where finite thermal relaxation times are important [12,13]. To counter this limitation, the Cattaneo–Christov heat flux model introduces thermal relaxation and frame indifferent heat transfer. This framework offers a more realistic description for polymer processing conditions [14–16]. The fluid behavior is further affected by magnetic damping, porous resistance, thermal stratification, and chemical reaction [17–20]. These effects indicate that a more complete formulation is required when studying extrusion flows and related manufacturing systems [21–24].

Traditional numerical approaches, such as finite difference schemes and collocation methods, have provided valuable results but remain dependent on mesh construction and may require careful initial estimates when applied to nonlinear boundary value problems [25,26]. In the present study, a physics informed neural formulation is adopted to model third grade viscoelastic flow with non-Fourier heat conduction and reactive transport [27–30]. The governing equations and boundary conditions are incorporated directly into a loss function, allowing the

---

* Corresponding author.

E-mail addresses: hamza.kazmi_22@sms.edu.pk (S.H.H. Kazmi), noor.muhammad@kfupm.edu.sa (N. Muhammad), taha.aziz@kfupm.edu.sa (T. Aziz), haitamb@kfupm.edu.sa (H.M.S. Bahaidarah).

https://doi.org/10.1016/j.icheatmasstransfer.2026.110850

Table 1
List of symbols, transport properties, and material parameters used in the formulation.

Nomenclature			
k_2	Chemical reaction rate constant	T_∞	Temperature far from the sheet
B_0	Magnetic flux density	$\beta_1, \beta_2, \beta_3$	Third grade viscosity coefficients
c_p	Specific heat (J/kg K)	k	Thermal conductivity (W/m K)
A_i	Rivlin Ericksen tensors	μ_0	Magnetic permeability (H/m)
λ_3	Third grade material modulus	b	Wall thermal stratification parameter
ν	Kinematic viscosity ($\mathrm{m^2/s}$)	D	Mass diffusivity
λ_1	First grade material modulus	β_T	Thermal expansion coefficient
T_w	Sheet temperature	ρ	Fluid density ($\mathrm{kg/m^3}$)
α	Thermal diffusivity ($\mathrm{m^2/s}$)	β_C	Solutal expansion coefficient
K_1	Permeability of porous medium	α_1, α_2	Normal stress coefficients
τ_0	Thermal relaxation time (s)	C_w	Wall concentration
g	Gravitational acceleration ($\mathrm{m/s^2}$)	a	Stretching rate
λ_2	Second grade material modulus	c	Ambient thermal stratification parameter
μ	Dynamic viscosity (Pa s)	P	Pressure
Q	Internal heat source/sink rate	C_∞	Ambient concentration
σ	Electrical conductivity (S/m)	τ	Cauchy stress tensor

Table 2
Conceptual comparison of existing modeling frameworks for polymer and viscoelastic flow heat transfer and the present PINN based non-Fourier third grade formulation.

Study category	Fluid model	Heat transfer model	Solution approach
PINN based polymer extrusion studies	Newtonian or weakly non-Newtonian model	Fourier heat conduction	Physics informed neural networks
PINN based viscoelastic flow studies	Second grade or Oldroyd type/Maxwell model	Fourier heat conduction	Physics informed neural networks
Non-Fourier heat transfer in viscoelastic flows	Newtonian or viscoelastic model	Cattaneo–Christov heat flux	Classical numerical or analytical methods
Present work	**Third grade viscoelastic fluid model**	**Cattaneo–Christov heat flux**	**PINN with BVP4C validation**

solution to be obtained without mesh generation while maintaining adherence to the underlying physical laws [31].

Although recent studies have demonstrated the successful use of physics informed and machine learning frameworks for coupled thermal and transport problems [32,33], and AI-driven optimization has been applied to complex non-Newtonian nanofluid systems [34], these approaches have not yet been extended to viscoelastic polymer processing. Likewise, investigations of thermal stratification and magnetic effects in nanofluid flows [35] highlight the importance of non-Fourier heat transport and buoyancy mechanisms in industrial energy systems.

In parallel, significant progress has been reported in the broader field of scientific machine learning and physics informed neural networks, with recent comprehensive reviews emphasizing their capability to solve nonlinear, multiscale partial differential equations arising in fluid mechanics and heat transfer [36–38]. More recent contributions have further explored adaptive and data driven PINN variants for improving convergence and robustness in stiff nonlinear systems, including dispersive and wave type equations [39–41]. Despite these advances, existing PINN based studies in thermal and transport modeling have predominantly focused on Newtonian or weakly non-Newtonian fluids under Fourier heat conduction assumptions.

However, to the best of our knowledge, there is currently no study that combines third grade viscoelastic modeling with Cattaneo–Christov heat conduction and physics informed neural networks within a stretching sheet geometry. The present work therefore provides a complementary contribution, enabling a consistent predictive framework that captures viscoelastic memory and finite speed thermal propagation, and thereby enhances the capability of existing thermal management strategies used in polymer extrusion and related manufacturing processes. A conceptual comparison with existing frameworks is summarized in Table 2.

The objectives of this study are threefold: (i) to reformulate the third grade viscoelastic boundary layer problem with finite speed heat conduction in a form suitable for physics informed neural implementation; (ii) to assess the accuracy of the neural solution by comparison with established numerical benchmarks; and (iii) to analyze the influence of magnetic, porous, viscoelastic, and reactive parameters on the resulting velocity, temperature, and concentration fields. Through this hybrid modeling strategy, the study aims to provide actionable insights for optimizing heat and mass transfer in extrusion and coating processes.

The remainder of the paper is organized as follows. Section 2 introduces the governing equations and constitutive relations for the third grade viscoelastic model with Cattaneo–Christov heat flux. Section 3 introduces the similarity transformations, which gives the nondimensional ODE system. Section 4 describes the physics informed neural formulation, including the loss structure and training procedure. Section 5 presents the numerical and neural results, together with their physical interpretation. Section 6 provides concluding remarks and discusses implications for polymer processing.

1. Mathematical model

This study considers a two dimensional, steady, laminar, and incompressible boundary layer flow of a third grade viscoelastic polymer melt over a stretching sheet. The formulation includes magnetohydrodynamic effects, porous resistance, thermal stratification, and a first order chemical reaction within the fluid. The stretching velocity of the sheet is prescribed as $u = ax$, where a denotes the stretching rate. The physical configuration, shown in Fig. 1, represents a standard model for analyzing thermal and material transport in extrusion and coating processes. The sheet is assumed impermeable and located at $y = 0$, with the polymer melt occupying the region $y > 0$. The x-axis is along the stretching sheet, while the y-axis is normal to the sheet.

A uniform transverse magnetic field is applied perpendicular to the flow, which generates a Lorentz force that alters the motion of the electrically conducting fluid. The velocity components $u(x, y)$ and $v(x, y)$ represent motion along the tangential and normal directions, respectively. The sheet temperature and concentration are fixed at $T = T_w$ and $C = C_w$, whereas the ambient temperature and concentration are $T \to T_\infty$ and $C \to C_\infty$, respectively. This configuration reflects polymer

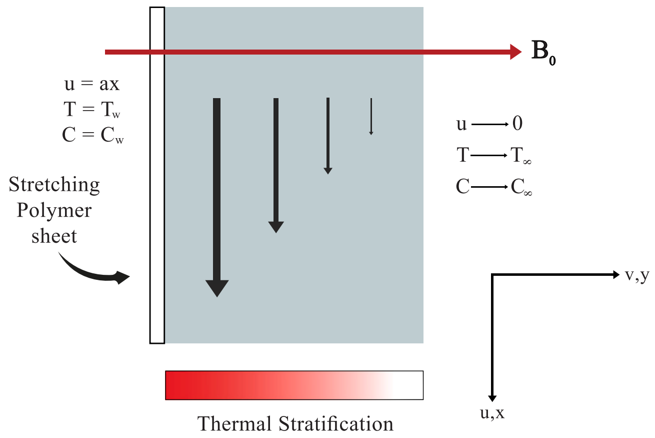

Fig. 1. Schematic representation of the steady third grade fluid flow over a stretching sheet, showing the stretching velocity $u = ax$, wall conditions for T and C, the transverse magnetic field B_0, and the presence of thermal stratification.

sheet extrusion framework, where stretching, magnetic effect, and heat and mass transfer jointly influence product quality. The parameters and symbols used throughout the formulation are listed in Table 1, and the physical configuration is illustrated in Fig. 1.

The stretching sheet configuration adopted in this study represents an idealized model of polymer extrusion and coating processes. While an industrial extrusion die involves finite length, complex geometry, pressure driven flow, and possible unsteady effects, the present model captures the dominant near wall shear, stretching, and heat transfer mechanisms that govern polymer sheet formation. Accordingly, the formulation is intended to provide reduced order insight into viscoelastic and thermal transport behavior under controlled stretching conditions rather than a detailed geometric representation of an industrial extrusion die.

2. Conservation principles

The present analysis deals with a steady, incompressible, two dimensional fluid flow. The governing equations are established using the fundamental conservation laws for mass, momentum, thermal energy, and chemical species. These governing relations are as follows:

The continuity equation

$$\frac{\partial u}{\partial x} + \frac{\partial v}{\partial y} = 0. \tag{1}$$

For a third grade viscoelastic material, the Cauchy stress tensor τ_{ij} takes the following form [42]:

$$\tau = -PI + \mu A_1 + \alpha_1 A_2 + \alpha_2 A_1^2 + \beta_1 A_3 + \beta_2(A_2 A_1 + A_1 A_2) + \beta_3(trA_1^2)A_1, \tag{2}$$

In Eq. (2), α_1 and α_2 represent the second grade material constants, whereas β_1, β_2, and β_3 are associated with the third grade properties of the fluid. The tensors A_i are given as

$$A_1 = (\nabla V) + (\nabla V)^T,$$

$$A_i = \frac{dA_{i-1}}{dt} + A_{i-1}(\nabla V) + (\nabla V)^T A_{i-1}, \quad \text{where} \quad i > 1, \tag{3}$$

the constitutive constraints are expressed as

$$\mu \geq 0, \quad \alpha_1 \geq 0, \quad |\alpha_1 + \alpha_2| \leq \sqrt{24\mu\beta_3}, \quad \beta_1 = \beta_2 = 0, \quad \beta_3 \geq 0, \tag{4}$$

substituting Eq. (4) in Eq. (2)

$$\tau = -PI + \mu A_1 + \alpha_1 A_2 + \alpha_2 A_1^2 + \beta_3(trA_1^2)A_1. \tag{5}$$

Under the boundary layer assumptions, the momentum equation takes the form:

$$\begin{aligned} u\frac{\partial u}{\partial x} + v\frac{\partial u}{\partial y} &= \nu\frac{\partial^2 u}{\partial y^2} + \lambda_1\Big(v\frac{\partial^3 u}{\partial y^3} + u\frac{\partial^3 u}{\partial x\partial y^2} + 3\frac{\partial u}{\partial x}\frac{\partial^2 u}{\partial y^2} + \frac{\partial v}{\partial y}\frac{\partial^2 u}{\partial y^2}\Big) \\ &\quad + 2\lambda_2\frac{\partial u}{\partial y}\frac{\partial^2 u}{\partial x\partial y} + 6\lambda_3\frac{\partial^2 u}{\partial y^2}\Big(\frac{\partial u}{\partial y}\Big)^2 \\ &\quad + g\beta_T(T - T_\infty) + g\beta_C(C - C_\infty) - \frac{\nu}{K_1}u - \frac{\sigma B_0^2}{\rho}u, \end{aligned} \tag{6}$$

$$\begin{aligned} &u = ax, \quad v = 0, \quad \text{at} \quad y = 0, \\ &u \to 0, \quad \frac{\partial u}{\partial y} \to 0, \quad \text{as} \quad y \to \infty. \end{aligned} \tag{7}$$

Here $a > 0$, $\nu = \mu/\rho$, $\lambda_1 = \alpha_1/\rho$, $\lambda_2 = \alpha_2/\rho$, and $\lambda_3 = \beta_3/\rho$.

The corresponding energy equation, expressed under the boundary layer assumptions, can be written as:

$$\begin{aligned} &\tau_0\Bigg(2u\frac{\partial T}{\partial x}\frac{\partial u}{\partial x} + u\frac{\partial T}{\partial x}\frac{\partial v}{\partial y} + v\frac{\partial u}{\partial y}\frac{\partial T}{\partial x} + u^2\frac{\partial^2 T}{\partial x^2} + v\frac{\partial T}{\partial y}\frac{\partial u}{\partial x} + v\frac{\partial T}{\partial y}\frac{\partial v}{\partial y} \\ &+ v^2\frac{\partial^2 T}{\partial y^2} + u\frac{\partial v}{\partial x}\frac{\partial T}{\partial y} + v\frac{\partial v}{\partial y}\frac{\partial T}{\partial y} + 2uv\frac{\partial^2 T}{\partial y\partial x}\Bigg) \\ &+ v\frac{\partial T}{\partial y} + u\frac{\partial T}{\partial x} = \alpha\frac{\partial^2 T}{\partial y^2} + \frac{\nu}{c_p}\left(\frac{\partial u}{\partial y}\right)^2 + \frac{\lambda_1}{c_p}\left(2\frac{\partial v}{\partial y}\left(\frac{\partial u}{\partial y}\right)^2 + 3\frac{\partial u}{\partial x}\left(\frac{\partial u}{\partial y}\right)^2\right) \\ &+ \frac{\lambda_3}{c_p}\left(8\left(\frac{\partial v}{\partial y}\right)^2\left(\frac{\partial u}{\partial x}\right)^2 + 2\left(\frac{\partial u}{\partial y}\right)^4\right) \\ &+ \frac{Q}{\rho c_p}(T - T_\infty) + \frac{\sigma B_0^2 u^2}{\rho c_p}, \end{aligned} \tag{8}$$

$$\begin{aligned} &T = T_w = T_0 + b\left(\frac{x}{l}\right), \quad \text{at} \quad y = 0, \\ &T \to T_\infty = T_0 + c\left(\frac{x}{l}\right), \quad \text{as} \quad y \to \infty. \end{aligned} \tag{9}$$

Here, the thermal diffusivity is defined as $\alpha = k/(\rho c_p)$.

The species concentration equation, expressed under the boundary layer framework, is written as:

$$u\frac{\partial C}{\partial x} + v\frac{\partial C}{\partial y} = D\frac{\partial^2 C}{\partial y^2} - k_2(C - C_\infty), \tag{10}$$

$$\begin{aligned} &C = C_w, \quad \text{at} \quad y = 0, \\ &C \to C_\infty, \quad \text{as} \quad y \to \infty. \end{aligned} \tag{11}$$

The Eqs. (1)–(11) collectively represent the conservation of mass, momentum, energy, and species concentration for a third grade viscoelastic fluid under MHD and reactive effects.

3. Similarity transformations

To simplify the dimensional governing equations, the following similarity variables are introduced. These transformations convert the original nonlinear PDE system into a non-dimensional ODE system, suitable for further analysis. The similarity relations are defined as

$$\begin{aligned} &u = axf'(\eta), \\ &v = -f(\eta)\sqrt{a\nu}, \\ &\eta = \sqrt{\frac{a}{\nu}}y, \end{aligned} \tag{12}$$

where a prime indicates differentiation with respect to η. These transformations are admissible since both η and the function $f(\eta)$ are smooth and possess the required degree of differentiability.

$$\theta(\eta) = \frac{T - T_\infty}{T_w - T_\infty}, \tag{13}$$

$$\phi(\eta) = \frac{C - C_\infty}{C_w - C_\infty}. \tag{14}$$

The non-dimensional temperature and concentration variables are introduced in Eqs. (13)–(14). After applying these definitions, the resulting dimensionless momentum equation together with its associated boundary conditions is written as

$$\begin{aligned} &f''' + ff'' - \lambda(ff^{(iv)} - 3f'f''') - f'^2 + 2Wif''^2 + 6\lambda_T Re^2 f''^2 f''' \\ &\quad - Mf' - P_m f' + Gr_T\theta + Gr_C\phi = 0, \end{aligned} \tag{15}$$

$$\begin{aligned} &f(0) = 0, \quad f'(0) = 1, && \text{at} \quad \eta = 0. \\ &f'(\eta) \to 0, \quad f''(\eta) \to 0, && \text{as} \quad \eta \to \infty. \end{aligned} \tag{16}$$

The non-dimensional energy equation and its associated boundary conditions can be written as

$$\begin{aligned} \theta'' - Pr\lambda_\tau &\left(ff'\theta' + f'^2(S+\theta) - 2\big(ff'\theta' - f^2\theta'' - ff''(S+\theta)\big) \right) \\ &- Prf'(S+\theta) + Prf\theta' \\ &+ PrEc\left(f''^2 + \lambda f'f''^2 + 8\lambda_T f'^4 + 2\lambda_T Re^2 f''^4 + Mf'^2 \right) \\ &+ Pr\alpha_T\theta = 0, \end{aligned} \tag{17}$$

$$\begin{aligned} &\theta(0) = 1, && \text{at} \quad \eta = 0, \\ &\theta(\eta) \to 0, && \text{as} \quad \eta \to \infty. \end{aligned} \tag{18}$$

The dimensionless concentration equation and its boundary conditions are given as follows

$$\phi'' + Sc(f\phi' - Kr\phi) = 0, \tag{19}$$

$$\begin{aligned} &\phi(0) = 1, && \text{at} \quad \eta = 0, \\ &\phi(\eta) \to 0, && \text{as} \quad \eta \to \infty. \end{aligned} \tag{20}$$

The governing equations Eqs. (15)–(20) are now expressed in terms of the following non-dimensional parameters, which show the relative effects of viscous, elastic, thermal, and diffusive transport phenomena. The non-dimensional parameters used in this study are listed in Table 3.

To ensure physical relevance, the dimensional parameters underlying the present non-dimensional formulation are linked to experimentally measured rheological and thermal properties of industrial polymer melts. Dynamic rheological data for LDPE grades indicate zero shear viscosity of order 10^4–10^5 Pa·s and relaxation times spanning 10^{-4}–10^2 s, which yield range Weissenberg numbers and thermal relaxation parameter under typical extrusion shear rates [43,44]. Such conditions invalidate a purely Newtonian description and require a viscoelastic constitutive framework. In addition, measured thermal activation energies ($E_a \approx 50$ kJ/mol) indicate the presence of finite thermal relaxation effects in polymer melts, thereby supporting the use of a Cattaneo–Christov non-Fourier heat flux model.

4. Solution methodology

This section outlines the numerical techniques used to obtain both the reference solution and the physics informed neural network (PINN) approximation of the reduced non-dimensional system. The boundary value problem is first solved using the `bvp4c` solver in MATLAB to obtain a reliable benchmark solution. A physics informed neural formulation is then developed to produce a mesh free approximation of the ODE system and to explore how the solution changes with the non-dimensional parameters.

4.1. Reference solution via `bvp4c`

To validate the PINN predictions, a numerical reference solution is obtained using the `bvp4c` solver in MATLAB. The reduced governing equations are first converted into a first order system by introducing auxiliary variables for the derivatives. The resulting boundary value problem is solved using the collocation method implemented in `bvp4c`. The solver employs adaptive mesh refinement until the default accuracy criteria are satisfied. This numerical solution provides a benchmark for assessing the accuracy of the PINN approximation.

4.2. PINN framework and solution strategy

To obtain a mesh free numerical approximation of the reduced equations, a physics informed neural network (PINN) is employed. In this formulation, the unknown similarity functions $f(\eta)$, $\theta(\eta)$, and $\phi(\eta)$ are represented by a neural network,

$$\big(f(\eta),\, \theta(\eta),\, \phi(\eta)\big) \;\approx\; \mathcal{N}(\eta; \boldsymbol{\omega}), \tag{21}$$

where $\eta \in [0, \eta_{\max}]$ denotes the similarity coordinate and $\boldsymbol{\omega}$ collects the trainable weights and biases. The governing equations and boundary conditions are imposed in a weak sense by minimizing a composite loss function that penalizes both the differential equation residuals and deviations from the prescribed boundary values.

4.2.1. Neural network architecture

A fully connected feed-forward neural network is constructed with a single scalar input and three outputs, as shown in Fig. 2. The input to the network is the similarity coordinate η, while the outputs approximate the dimensionless velocity, temperature, and concentration profiles,

$$\eta \;\mapsto\; \mathcal{N}(\eta; \boldsymbol{\omega}) = \big(f_{\mathrm{NN}}(\eta),\, \theta_{\mathrm{NN}}(\eta),\, \phi_{\mathrm{NN}}(\eta)\big). \tag{22}$$

The network consists of an input layer, four hidden layers, and one output layer. Each hidden layer contains 64 neurons and employs the hyperbolic tangent (`tanh`) activation function. The implementation is carried out in `PyTorch`, with Xavier initialization applied to the weights to enhance training stability.

Automatic differentiation is employed to compute the required derivatives of the network outputs with respect to η, including f'_{NN}, f''_{NN}, f'''_{NN}, $f^{(iv)}_{\mathrm{NN}}$, θ'_{NN}, θ''_{NN}, and ϕ'_{NN}, ϕ''_{NN}. These derivatives are used to evaluate the residuals of the momentum, energy, and concentration equations in the PINN formulation.

The network architecture was selected to balance approximation capability and computational efficiency. A depth of four hidden layers with 64 neurons per layer was sufficient to capture the smooth yet highly nonlinear behavior of the coupled momentum, energy, and concentration equations without inducing training instability or excessive computational cost. The tanh activation function was employed due to its smoothness and favorable performance in representing boundary layer type solutions involving higher order spatial derivatives. Increasing network depth or width did not yield noticeable improvements in accuracy for the present problem, whereas smaller architectures exhibited reduced convergence robustness.

The PINN employed in this work uses a standard residual minimization framework with uniform collocation points and soft enforcement of boundary conditions through the loss function. In the broader PINN literature, more advanced strategies are sometimes used, including adaptive loss weighting to balance PDE and boundary residuals, adaptive sampling to concentrate points in regions of larger error, and hard enforcement of boundary or far field conditions through trial solution constructions. In the present study, a baseline PINN architecture is intentionally adopted to provide a clear and reproducible benchmark against the classical `bvp4c` solver for the reduced similarity equations. Since the governing equations are smooth and only moderately stiff over the parameter ranges considered, stable convergence is achieved without these additional techniques, which remain natural extensions for future work.

Table 3
Dimensionless groups arising from the similarity reduction, together with their physical interpretation in the context of viscoelastic polymer extrusion and non-Fourier heat transfer.

Dimensionless parameters and physical interpretation			
Wi	Weissenberg number	$Wi = \frac{\lambda_2 a}{\nu}$	Measures elastic memory effects relative to the imposed deformation rate.
Gr_C	Solutal Grashof number	$Gr_C = \frac{g\beta_C(C_w - C_\infty)}{a^2 l}$	Quantifies buoyancy forces induced by concentration gradients relative to viscous forces.
M	Magnetic interaction parameter	$M = \frac{\sigma B_0^2}{a\rho}$	Represents magnetic damping effects opposing fluid motion and modifying momentum transport.
Sc	Schmidt number	$Sc = \frac{\nu}{D}$	Ratio of momentum diffusivity to mass diffusivity, governing species transport thickness.
λ_T	Third-grade fluid parameter	$\lambda_T = \frac{a\lambda_3}{l^2}$	Accounts for higher order nonlinear viscoelastic effects characteristic of third grade fluids.
Re	Reynolds number	$Re = \frac{al^2}{\nu}$	Ratio of inertial to viscous forces, characterizing flow regime intensity.
α_T	Heat generation and absorption parameter	$\alpha_T = \frac{Q}{a\rho c_p}$	Represents internal heat generation or absorption within the polymer melt.
Pr	Prandtl number	$Pr = \frac{\nu}{\alpha}$	Ratio of momentum diffusivity to thermal diffusivity, controlling thermal boundary layer thickness.
P_m	Porous medium parameter	$P_m = \frac{\nu}{aK_1}$	Quantifies flow resistance due to the porous substrate.
Ec	Eckert number	$Ec = \frac{a^2 l^2}{(T_w - T_\infty)c_p}$	Measures viscous dissipation converting kinetic energy into thermal energy.
λ_τ	Thermal relaxation parameter	$\lambda_\tau = \tau_0 a$	Characterizes finite speed heat propagation effects under non-Fourier heat conduction.
Gr_T	Thermal Grashof number	$Gr_T = \frac{g\beta_T(T_w - T_\infty)}{a^2 l}$	Quantifies buoyancy forces induced by temperature gradients.
λ	Second grade fluid parameter	$\lambda = \frac{\lambda_1 a}{\nu}$	Represents elastic normal stress effects associated with second grade fluid behavior.
S	Thermal stratification parameter	$S = \frac{c}{b-c}$	Measures the strength of thermal stratification between the wall and ambient fluid.
Kr	Chemical reaction parameter	$Kr = \frac{k_2}{a}$	Governs the strength of homogeneous first order chemical reactions.

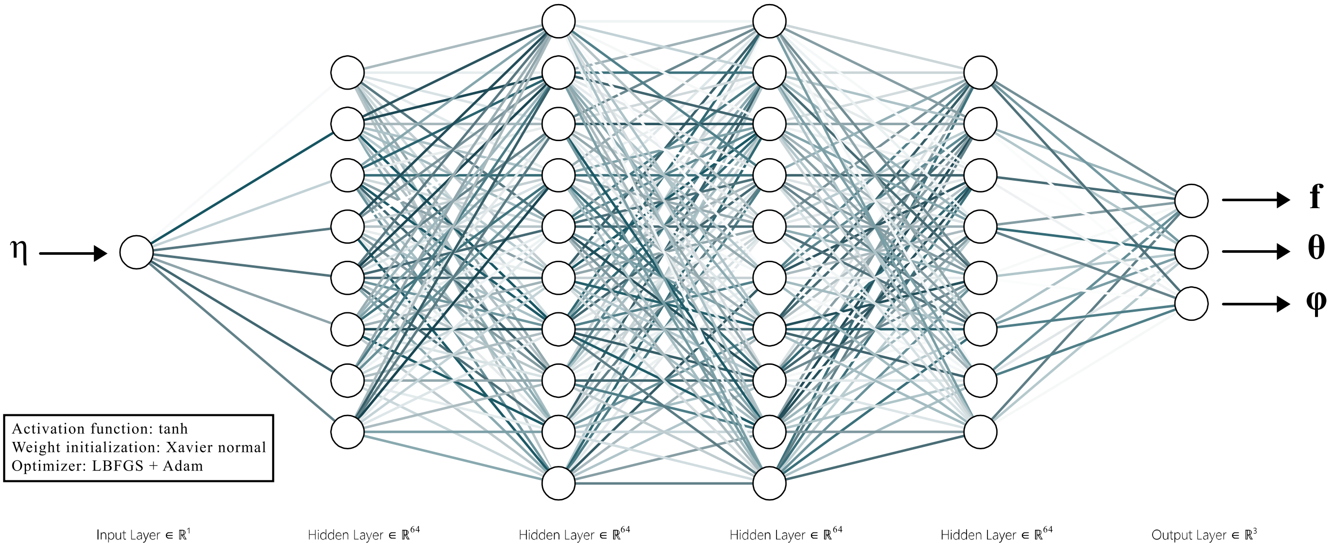

Fig. 2. Neural network architecture used in the PINN formulation. The similarity variable η is provided as input and propagates through four hidden layers of 64 neurons with tanh activation. The outputs correspond to the stream function $f(\eta)$, temperature $\theta(\eta)$, and concentration $\phi(\eta)$. Weights are initialized using Xavier normal initialization, and the model is optimized using an initial Adam phase followed by the L-BFGS optimizer.

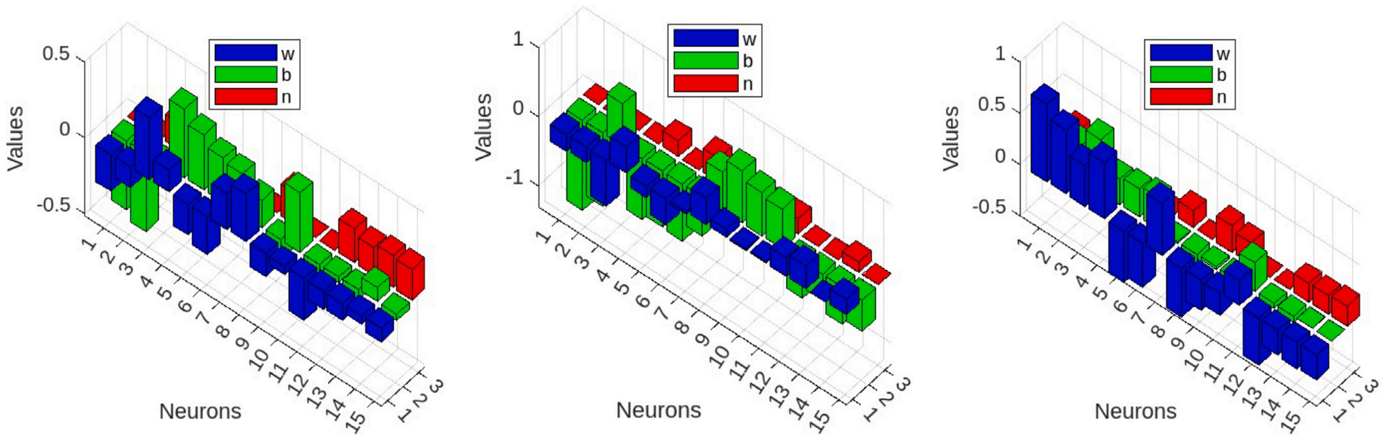

(a) Low magnitude regime (b) Moderate regime (c) High magnitude regime

Fig. 3. Evolution of the learned PINN parameters (w, b, n) across different stages of training. The transition from the low to high magnitude regimes reflects the network's progressive adaptation to the encoded nonlinear viscoelastic transport physics.

4.2.2. *Collocation and boundary sampling*

The computational domain in the similarity coordinate is taken as $\eta \in [0, \eta_{\max}]$ with $\eta_{\max} = 10$, which is sufficiently large to capture the asymptotic decay of the boundary layer profiles. Three categories of training points are employed:

- **Left boundary points** at $\eta = 0$: $N_{\rm L} = 500$ samples enforcing

  $$f(0) = 0, \qquad f'(0) = 1, \qquad \theta(0) = 1, \qquad \phi(0) = 1.$$

- **Right boundary points** at $\eta = \eta_{\max}$: $N_{\rm R} = 500$ samples enforcing

  $$f'(\eta_{\max}) = 0, \qquad \theta(\eta_{\max}) = 0, \qquad \phi(\eta_{\max}) = 0,$$

  providing a finite domain approximation of the far field conditions.
- **Interior collocation points**: $N_{\rm r} = 10{,}000$ uniformly distributed points in $[0, \eta_{\max}]$ used to enforce the differential equations throughout the domain.

All training points are assembled into mini batches using the `DataLoader` utility in `PyTorch` during optimization.

4.2.3. *Physics informed loss function*

Let $R_f(\eta)$, $R_\theta(\eta)$, and $R_\phi(\eta)$ denote the residuals of the dimensionless momentum, energy, and concentration equations, respectively, obtained by substituting the neural network approximations $(f_{\rm NN}, \theta_{\rm NN}, \phi_{\rm NN})$ and their derivatives into Eqs. (15), (17), (19). For illustration, the residual of the momentum equation takes the form

$$\begin{aligned} R_f(\eta) = {} & f'''_{\rm NN} - f'^2_{\rm NN} + f_{\rm NN} f''_{\rm NN} + \lambda\left(3 f'_{\rm NN} f'''_{\rm NN} - f_{\rm NN} f^{(iv)}_{\rm NN}\right) + 2Wi\left(f''_{\rm NN}\right)^2 \\ & + 6Re^2 \lambda_T \left(f''_{\rm NN}\right)^2 f'''_{\rm NN} \\ & - M f'_{\rm NN} - P_m f'_{\rm NN} + Gr_T \theta_{\rm NN} + Gr_C \phi_{\rm NN}, \end{aligned} \tag{23}$$

with analogous expressions defining $R_\theta(\eta)$ and $R_\phi(\eta)$ from the energy and concentration equations.

The physics informed loss consists of an ODE residual component and a boundary condition component,

$$\mathcal{L}_{\rm tot} = \mathcal{L}_{\rm ODE} + \mathcal{L}_{\rm BC}. \tag{24}$$

The ODE residual loss is defined as the mean squared error of the three residuals over the interior collocation points,

$$\mathcal{L}_{\rm ODE} = \frac{1}{N_{\rm r}} \sum_{i=1}^{N_{\rm r}} \left(R_f(\eta_i)^2 + R_\theta(\eta_i)^2 + R_\phi(\eta_i)^2 \right), \tag{25}$$

where $\{\eta_i\}_{i=1}^{N_{\rm r}}$ denote the interior sampling locations.

The boundary condition loss penalizes deviations from the prescribed conditions at $\eta = 0$ and $\eta = \eta_{\max}$. In compact form,

$$\begin{aligned} \mathcal{L}_{\rm BC} = {} & \frac{1}{N_{\rm L}} \sum_{i=1}^{N_{\rm L}} \Big[(f_{\rm NN}(0) - 0)^2 + (f'_{\rm NN}(0) - 1)^2 + (\theta_{\rm NN}(0) - 1)^2 \\ & + (\phi_{\rm NN}(0) - 1)^2 \Big] \\ & + \frac{1}{N_{\rm R}} \sum_{i=1}^{N_{\rm R}} \Big[(f'_{\rm NN}(\eta_{\max}) - 0)^2 + (\theta_{\rm NN}(\eta_{\max}) - 0)^2 + (\phi_{\rm NN}(\eta_{\max}) - 0)^2 \Big], \end{aligned} \tag{26}$$

consistent with Eqs. (16), (18), (20). The total loss $\mathcal{L}_{\rm tot}$ is minimized with respect to the network parameters $\boldsymbol{\omega}$.

4.2.4. *Training strategy and implementation*

The network is trained using gradient based optimization in `PyTorch`. The weights are initialized using Xavier initialization with a fixed random seed to ensure reproducibility. Training is performed in two stages: an initial pre-training phase using the Adam optimizer to reach a suitable region of the parameter space, followed by refinement with the quasi-Newton LBFGS optimizer to accelerate convergence of the loss function. The evolution of the network parameters during training is illustrated in Fig. 3.

In the present simulations, the similarity domain is taken as $[0, 10]$, with $N_{\rm L} = N_{\rm R} = 500$ boundary samples and $N_{\rm r} = 10{,}000$ interior collocation points. The network is trained for 6000 epochs, during which the loss history is monitored continuously and model checkpoints are saved periodically to enable resumption of long runs. After convergence, the PINN predictions for $f(\eta)$, $\theta(\eta)$, and $\phi(\eta)$ are processed to compute the velocity, temperature, and concentration profiles, as well as derived quantities such as the skin friction and Sherwood numbers. For selected parameter sets, the PINN results are compared with the classical `bvp4c` solution to assess accuracy.

4.2.5. *Training performance and convergence analysis*

The evolution of the training loss reflects the stability and overall performance of the optimization process. Fig. 4 shows the total loss on a logarithmic scale over 6000 training epochs. The loss steadily decreases, showing that the optimization remains stable and that the governing equations and boundary conditions are being satisfied.

To examine the relative contribution of each loss component, Fig. 5 compares the total loss with its ODE residual and boundary condition terms during the initial training stage. The loss is dominated by the ODE residual, and the boundary term stabilizes once the conditions are met. This is typical of PINN training, where the boundaries converge first

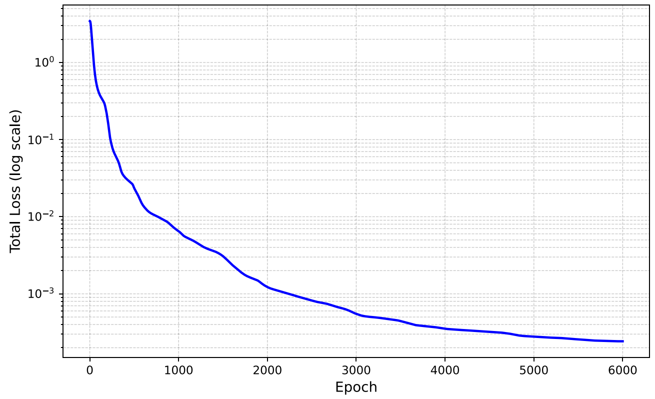

Fig. 4. Log scale convergence of the PINN during training. The steady drop in total loss over 6000 epochs indicates stable optimization and proper enforcement of both the ODE residuals and the boundary conditions.

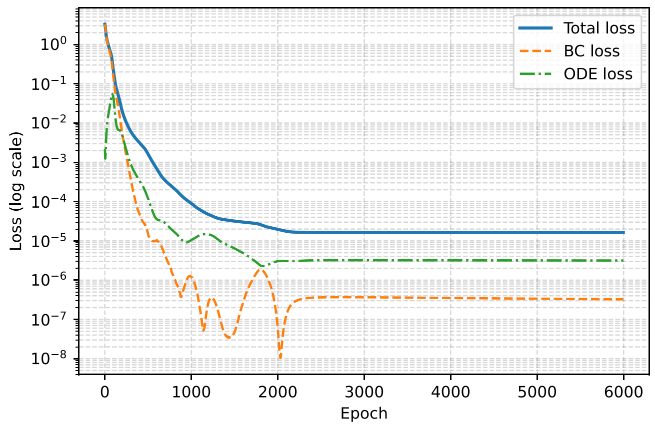

Fig. 5. Convergence history of the total loss, ODE loss, and boundary condition loss during the training of the physics informed neural network, shown on a logarithmic scale.

and the interior improves slowly. Overall, the results confirm that the training yields a converged model that accurately resolves the reduced non dimensional system.

4.3. *Error analysis*

The accuracy of the PINN formulation is assessed by comparing its predictions with the reference `bvp4c` solution for the three profiles. Figs. 6–8 present the pointwise absolute errors for the velocity gradient $f'(\eta)$, the temperature field $\theta(\eta)$, and the concentration field $\phi(\eta)$, respectively, plotted on a logarithmic scale. The errors remain within $\mathcal{O}(10^{-3})$—$\mathcal{O}(10^{-5})$ across the computational domain, with the largest deviations occurring in the far field region where the profiles decay rapidly. The uniform low magnitude errors confirm that the trained PINN captures the essential boundary layer behavior and provides a reliable approximation to the reduced system.

4.3.1. *Error norms*

Alongside the pointwise error plots, Table 4 lists the maximum and L_2 error norms for the three fields. The results show small errors in all cases, with the velocity gradient having the smallest deviations and the temperature field showing somewhat larger variations because of stronger nonlinear coupling in the energy equation. These measures confirm that the PINN matches the benchmark solution with good accuracy across the domain.

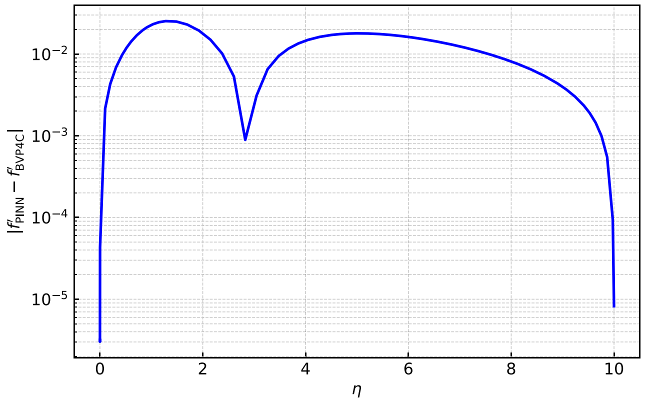

Fig. 6. Pointwise absolute error between the PINN solution and the `bvp4c` benchmark for the velocity gradient $f'(\eta)$. The error stays within $\mathcal{O}(10^{-3})$ across the domain, showing a reliable and converged PINN solution.

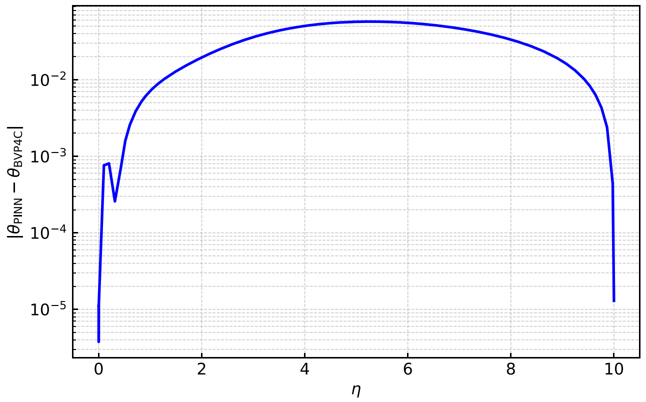

Fig. 7. Pointwise absolute error between the PINN and `bvp4c` solutions for the temperature field $\theta(\eta)$. The errors remain within $\mathcal{O}(10^{-3})$ across the computational domain.

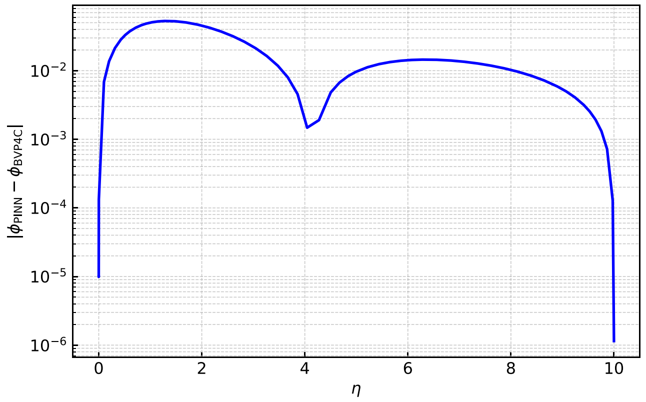

Fig. 8. Pointwise absolute error between the PINN and `bvp4c` results for the concentration field $\phi(\eta)$, with errors between $\mathcal{O}(10^{-3})$ over the domain.

4.3.2. *Pointwise comparison*

The point-wise comparison in Table 5 and Figs. 9–11 shows that the PINN solution is in excellent agreement with the `bvp4c` reference across the entire boundary layer region. The agreement is particularly strong near the wall and within the core of the layer, where the gradients are largest. Minor discrepancies appear only in the far field region, where all dependent variables decay to zero and the governing

Table 4
Maximum and L_2 error norms for $f'(\eta)$, $\theta(\eta)$, and $\phi(\eta)$, showing how the PINN solution differs from the `bvp4c` reference across the domain.

Quantity	Max error	L_2 error
$f'(\eta)$	2.5264×10^{-2}	4.3141×10^{-2}
$\theta(\eta)$	5.7472×10^{-2}	1.1921×10^{-1}
$\phi(\eta)$	5.2901×10^{-2}	7.5439×10^{-2}

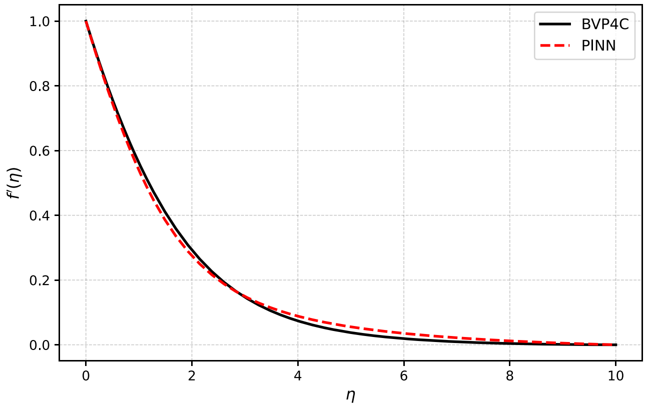

Fig. 9. Comparison of the `bvp4c` reference solution and the PINN prediction for the velocity gradient $f'(\eta)$, illustrating the close agreement of both profiles throughout the boundary layer.

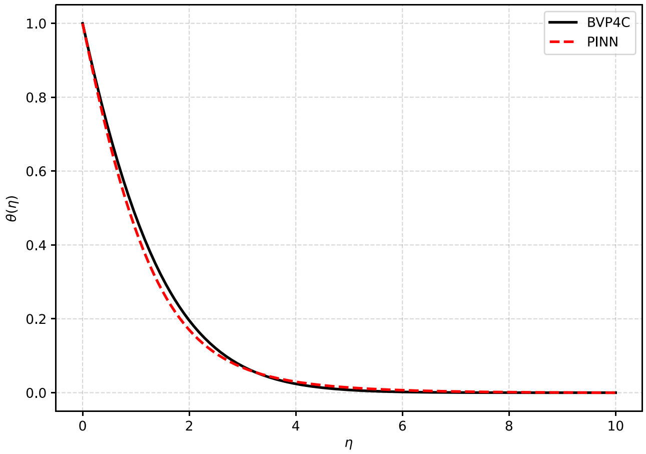

Fig. 10. Comparison between the `bvp4c` reference solution and the PINN prediction for the temperature field $\theta(\eta)$, showing close agreement throughout the computational domain.

equations become weakly sensitive. These differences remain small and consistent with the error levels reported in the log scale plots, confirming that the PINN accurately captures the full qualitative behavior and quantitative magnitude of all three similarity profiles.

4.3.3. Wall quantity comparison

The accuracy of the PINN in capturing wall driven transport is further assessed through the quantities $f''(0)$, C_f, $C_f\sqrt{Re}$, and Sh_x. Table 6 shows that the PINN matches the wall shear and skin-friction values very closely, with differences of only about 2%. This means the model captures the sharp changes in momentum near the sheet effectively.

In contrast, larger discrepancies are observed for the concentration gradient $\phi'(0)$ and the corresponding Sherwood number Sh_x. While pointwise field errors remain small throughout the domain, wall-derivative quantities such as $\phi'(0)$ are more sensitive to far field enforcement, leading to comparatively larger relative deviations. Nevertheless, the PINN retains the correct magnitude and trend of the mass transfer response, as illustrated in Fig. 12, and remains consistent with the physical behavior expected for reactive boundary layer flows.

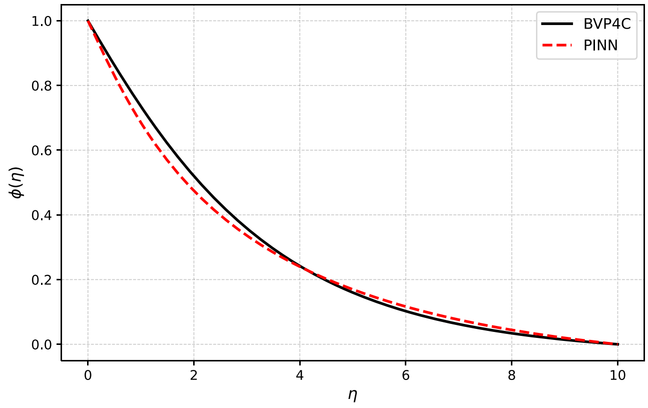

Fig. 11. Comparison of the `bvp4c` solution and the PINN prediction for the concentration profile $\phi(\eta)$, illustrating close agreement throughout the boundary layer region.

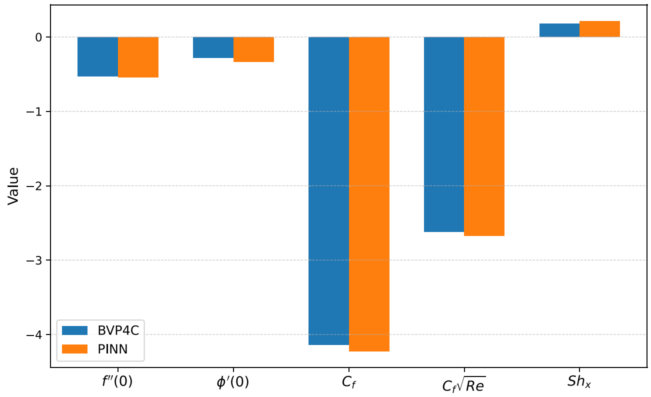

Fig. 12. Comparison of wall quantities obtained from the `bvp4c` reference solution and the PINN model for the baseline parameter set, considering C_f and Sh_x.

4.4. Numerical robustness and computational cost

Although the PINN framework incurs a higher one-time training cost, it offers clear robustness advantages when exploring wide ranges of non-dimensional parameters. In the present study, the trained PINN consistently produced smooth and physically admissible velocity, temperature, and concentration profiles across all tested parameter regimes, without numerical singularities or loss of stability. In contrast, classical boundary value solvers such as `bvp4c` are known to be sensitive to initial guesses and parameter magnitudes, and may experience convergence difficulties for strongly nonlinear viscoelastic parameter combinations. This robustness makes the PINN well suited for parametric exploration of highly nonlinear polymer flow models.

The convergence behavior of the PINN during training is illustrated in Fig. 13, which shows the decay of the total loss with increasing training time. All runtimes reported in Table 7 correspond to representative simulations performed on the same workstation using the solver settings described in the text. While the classical `bvp4c` solver remains effective for single-parameter benchmarking, the trained PINN enables rapid inference and supports repeated evaluations and parametric studies with negligible additional computational cost.

Table 5
Pointwise comparison of the PINN predictions and the bvp4c reference solutions for $f'(\eta)$, $\theta(\eta)$, and $\phi(\eta)$ at selected collocation points, illustrating the local accuracy of the PINN across the computational domain.

η	f'_{BVP4C}	f'_{PINN}	θ_{BVP4C}	θ_{PINN}	ϕ_{BVP4C}	ϕ_{PINN}
0.000000	1.000000e+00	9.999970e−01	1.000000e+00	9.999890e−01	1.000000e+00	9.999900e−01
1.031452	5.513204e−01	5.281740e−01	4.647895e−01	4.572960e−01	7.276560e−01	6.770000e−01
1.923883	3.083103e−01	2.889300e−01	2.111179e−01	1.926810e−01	5.343736e−01	4.875860e−01
3.046985	1.424611e−01	1.455650e−01	6.892917e−02	3.213400e−02	3.519480e−01	3.307670e−01
4.992467	3.778190e−02	5.566700e−02	7.997728e−03	−4.916600e−02	1.603612e−01	1.699830e−01
7.872614	4.450243e−03	1.310100e−02	2.281663e−04	−3.509700e−02	3.708478e−02	4.788800e−02
10.000000	9.094947e−13	−8.000000e−06	9.094947e−13	−1.300000e−05	9.094947e−13	−1.000000e−06

Table 6
Comparison of wall-shear $f''(0)$, concentration gradient $\phi'(0)$, skin-friction C_f, modified skin-friction $C_f\sqrt{Re}$, and Sherwood number Sh_x between the bvp4c and PINN solutions for the baseline parameter set.

Quantity	BVP4C	PINN	Absolute error	Relative error
$f''(0)$	−0.53015051	−0.54079755	0.01064704	0.0201
$\phi'(0)$	−0.28159366	−0.33319753	0.05160387	0.1832
C_f	−4.13922658	−4.22287872	0.08365214	0.0201
$C_f\sqrt{Re}$	−2.61787675	−2.67077946	0.05290271	0.0202
Sh_x	0.17809547	0.21073252	0.03263705	0.1832

Table 7
Measured wall-clock runtimes for the classical bvp4c solver and the proposed PINN framework.

Method	Runtime (s)
bvp4c (MATLAB)	21.234897
PINN training	10 027.20
PINN inference	$\sim 10^{-3}$

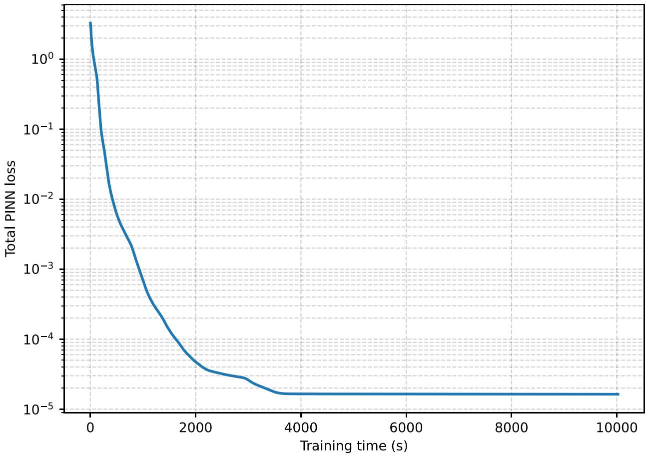

Fig. 13. Convergence behavior of the PINN during training, showing the decay of the total loss as a function of wall clock training time. After an initial transient phase, the loss decreases rapidly and stabilizes, indicating robust convergence of the network.

4.4.1. Far field truncation sensitivity

Since the physical boundary conditions are posed at $\eta \to \infty$, the PINN is trained on a truncated domain $\eta \in [0, \eta_{\max}]$. To verify that the truncation does not influence the computed wall quantities, a far field sensitivity study is performed by repeating the training for $\eta_{\max} = 8, 10, 12$, and 14 while keeping the network architecture, collocation sampling, and optimizer settings fixed.

Fig. 14 shows that the far-field residuals remain small and nearly unchanged for $\eta_{\max} \geq 10$, indicating that the solution is insensitive to further domain extension. Table 8 summarizes the corresponding wall derivatives and far-field residual values. The negligible variations in $f''(0)$, $-\theta'(0)$, and $-\phi'(0)$, together with near-zero far-field residuals, confirm that $\eta_{\max} = 10$ is sufficient for the present parameter set.

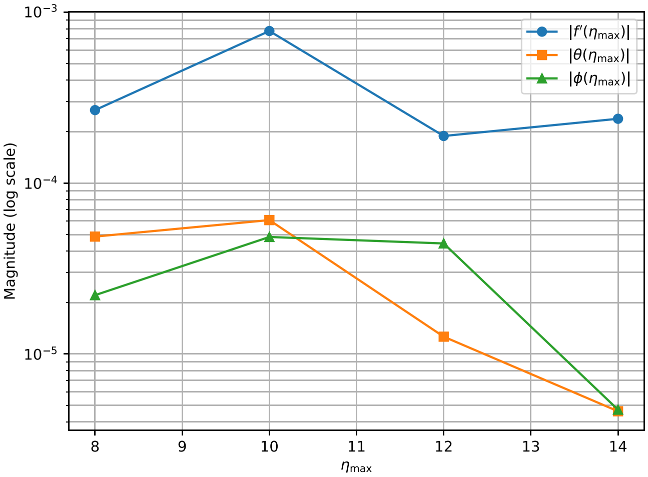

Fig. 14. Log-scale variation of the far-field residual magnitudes $|f'(\eta_{\max})|$, $|\theta(\eta_{\max})|$, and $|\phi(\eta_{\max})|$ with respect to the truncated domain size $\eta_{\max}$.

5. Results, validation, and transport behavior

This section presents the transport characteristics of the third grade viscoelastic boundary layer by examining the velocity, temperature, and concentration fields obtained from the similarity formulation. The results show how momentum, thermal, and solutal transport respond to the combined effects of viscoelasticity, magnetic effect, porous resistance, thermal stratification, and chemical reactivity. In addition to the field profiles, wall quantities of engineering relevance, such as the skin-friction and Sherwood numbers, are evaluated to characterize near wall momentum and mass transfer behavior. The discussion relates these trends to polymer extrusion, where control of thermal and rheological conditions is important for maintaining sheet stability and product quality.

5.1. Velocity behavior

The effects of viscoelasticity, MHD, porous resistance, and thermal buoyancy on the dimensionless velocity gradient $f'(\eta)$ are shown in Figs. 15–23. The profiles demonstrate how momentum transport responds to the influences of stretching, elastic stresses, and damping mechanisms within the third grade fluid.

Taken together, the velocity profiles in Figs. 15–23 show a consistent response to the governing parameters. Thermal and solutal buoyancy, represented by Gr_T and Gr_C, increase near wall acceleration, while the magnetic parameter M and the porous resistance P_m damp the motion and reduce the thickness of the momentum layer. The viscoelastic terms λ, λ_T, and Wi increase momentum transport by

Table 8

Sensitivity of key wall quantities and far-field residuals to the truncated computational domain size $\eta_{\max}$ (baseline: $\eta_{\max} = 10$).

$\eta_{\max}$	$f''(0)$	$-\theta'(0)$	$-\phi'(0)$	$f'(\eta_{\max})$	$\theta(\eta_{\max})$	$\phi(\eta_{\max})$
8	−0.804013	2.288726	0.714869	2.67×10^{-4}	-4.86×10^{-5}	-2.21×10^{-5}
10	−0.803961	2.288840	0.714719	-7.77×10^{-4}	6.07×10^{-5}	4.84×10^{-5}
12	−0.803908	2.289076	0.714607	-1.89×10^{-4}	-1.26×10^{-5}	-4.43×10^{-5}
14	−0.803954	2.288944	0.714651	-2.38×10^{-4}	-4.62×10^{-6}	-4.72×10^{-6}

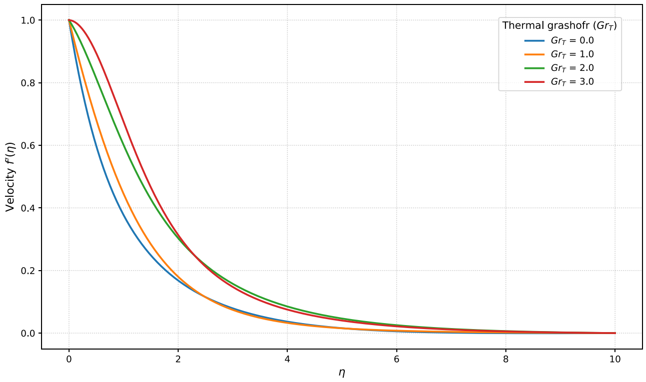

Fig. 15. Influence of Gr_T on $f'(\eta)$ for selected values of Gr_T, showing an increase in buoyancy driven acceleration with larger Gr_T.

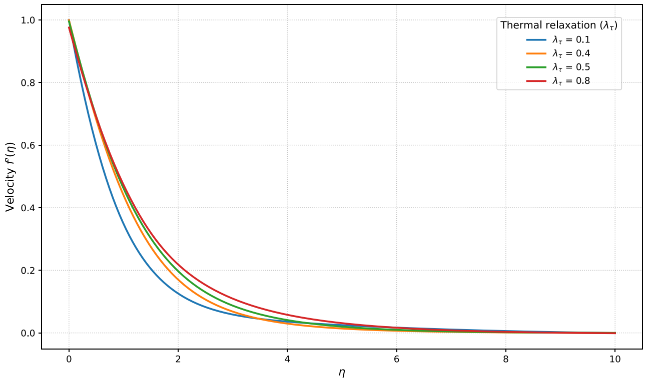

Fig. 16. Influence of λ_τ on $f'(\eta)$, illustrating the reduction in wall driven momentum transport as λ_τ increases.

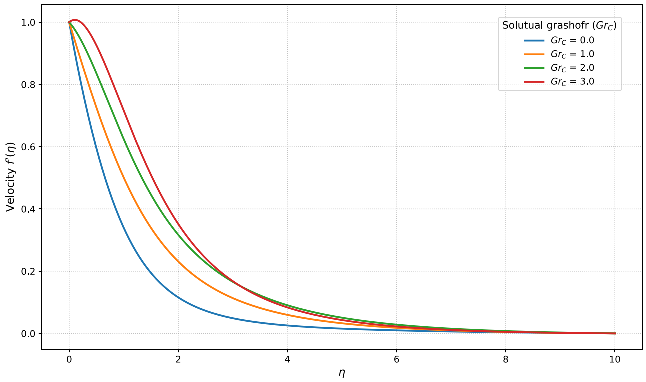

Fig. 17. Influence of Gr_C on $f'(\eta)$ for selected values of Gr_C, illustrating the enhancement of buoyancy induced momentum transport with increasing Gr_C.

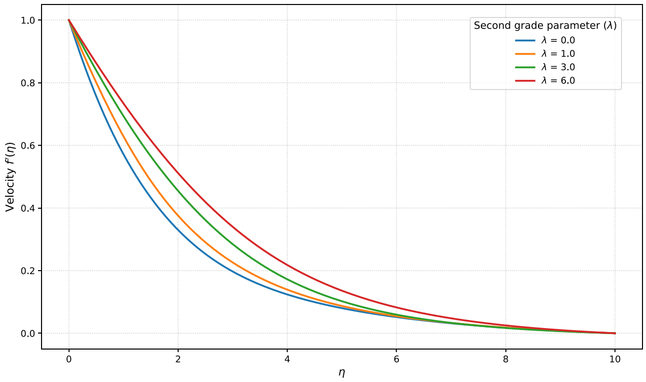

Fig. 18. Variation of $f'(\eta)$ for selected values of λ, showing enhanced wall driven momentum transport as λ increases.

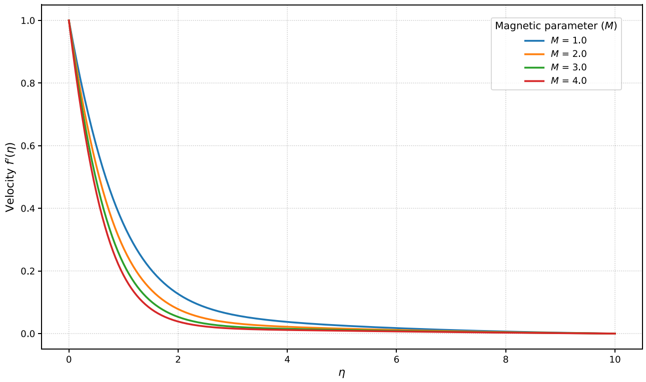

Fig. 19. Profiles of $f'(\eta)$ for selected values of M, showing a monotonic suppression of near wall transport with increasing M. The damping induced by larger M is consistent with magnetically moderated flow used in controlled polymer processing.

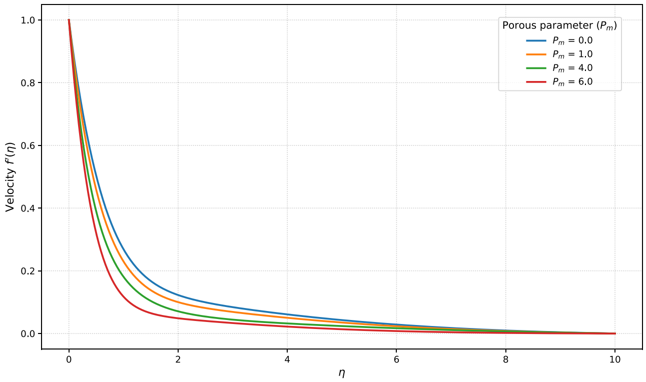

Fig. 20. Profiles of $f'(\eta)$ for selected values of P_m, showing reduced momentum transport as P_m increases. The trend reflects the damping imposed by a resistive substrate, relevant where the sheet interacts with porous or frictional supports.

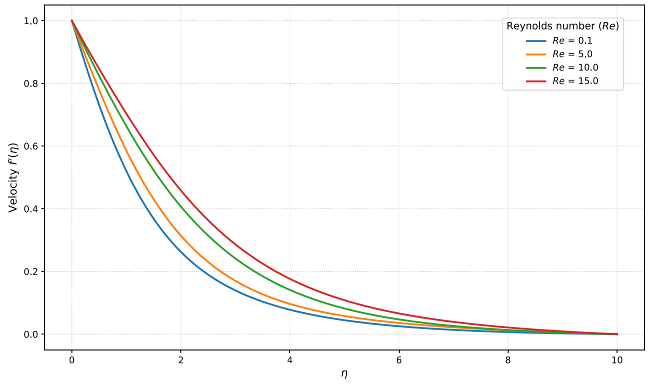

Fig. 21. Profiles of $f'(\eta)$ for selected values of Re, showing increased inertial transport and a slower decay of $f'(\eta)$ as Re increases.

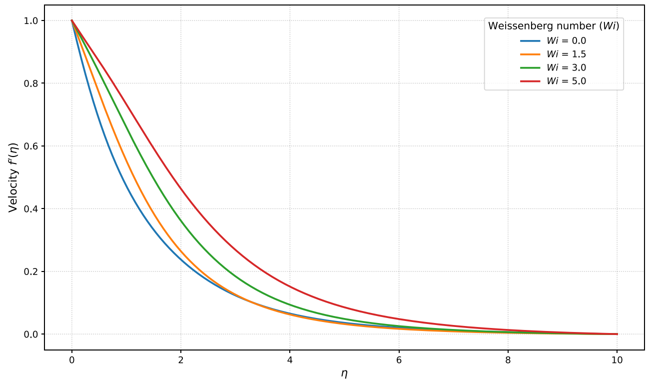

Fig. 22. Profiles of $f'(\eta)$ for selected values of Wi, showing stronger elastic effects and a slower decay of $f'(\eta)$ at larger Wi. This trend corresponds to the increased stretch induced response of viscoelastic melt flows.

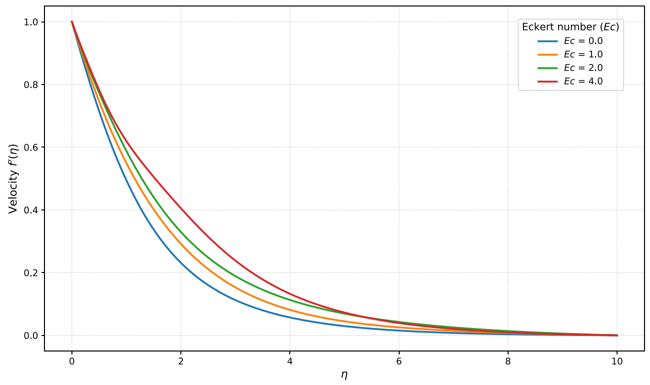

Fig. 23. Profiles of $f'(\eta)$ for increasing Ec values, showing an increase in $f'(\eta)$. Higher Ec lowers resistance to deformation because the heat generated by shear motion softens the material, a characteristic of heated viscoelastic melts.

strengthening the elastic stresses produced by sheet stretching. Increasing Re widens the momentum layer through inertial effects, and larger Ec produces a slight rise in $f'(\eta)$ because heat generated during shear motion softens the material. For all parameter values, the profiles are smooth and monotonic, and no numerical irregularities or nonphysical behavior are observed within the computational domain.

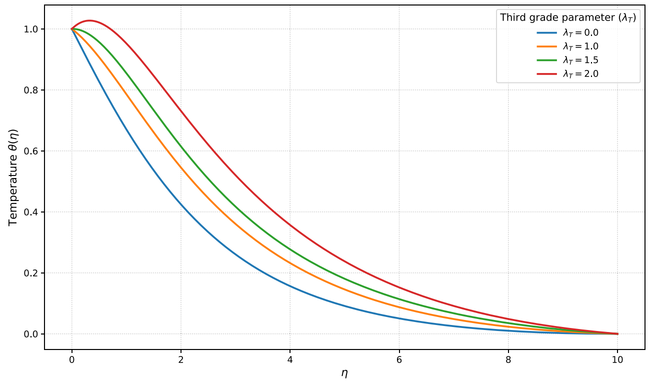

Fig. 24. Temperature profiles $\theta(\eta)$ for different values of the third-grade parameter λ_T. Larger λ_T produces a slower decay of $\theta(\eta)$ and a thicker thermal boundary layer.

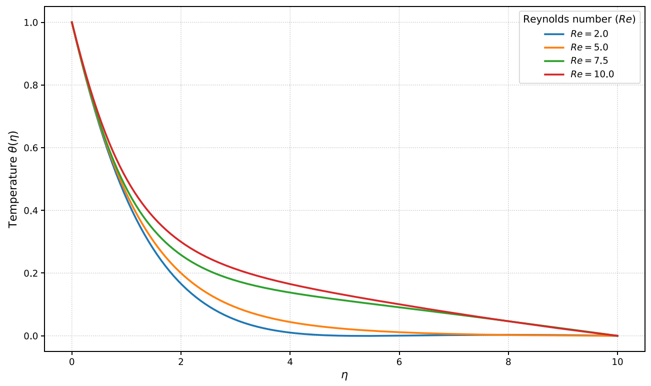

Fig. 25. Profiles of $\theta(\eta)$ for selected values of Re, showing a thinning of the thermal layer and faster decay of $\theta(\eta)$ as inertial effects increase.

5.2. Temperature behavior

The temperature profiles in Figs. 24–31 show how the thermal boundary layer responds to changes in the viscoelastic, thermal, and magnetic parameters. In all cases, $\theta(\eta)$ decreases smoothly away from the sheet, and the decay rate varies according to the underlying transport mechanisms. Increasing the third grade parameter λ_T, the Weissenberg number Wi, or the Eckert number Ec produces a thicker thermal layer, consistent with greater heat retention due to elastic stresses and viscous dissipation. A similar trend is observed when the magnetic parameter M or the heat generation coefficient $\alpha_T > 0$ is increased, since both mechanisms act to slow the removal of thermal energy from the near wall region. In contrast, larger Reynolds numbers and stronger thermal relaxation λ_τ accelerate the decay of the temperature field, indicating more effective convective transport and the delay introduced by non-Fourier conduction, respectively. The effect of thermal stratification S is also noticeable. When S increases, the temperature difference between the wall and the surrounding fluid becomes smaller. As a result, the driving force for heat transfer is reduced, and a slight dip appears in the temperature profile, which is typical in stratified boundary layers.

Taken together, these results provide a coherent picture of the thermal response of the third grade viscoelastic fluid under non–Fourier heat conduction. The profiles remain smooth and well behaved across all parameter ranges, and the observed trends are consistent with established behavior of stretched surface flows and polymer melt heating. The combined influence of elastic stresses, thermal relaxation, magnetic damping, and dissipation offers a physically plausible description of

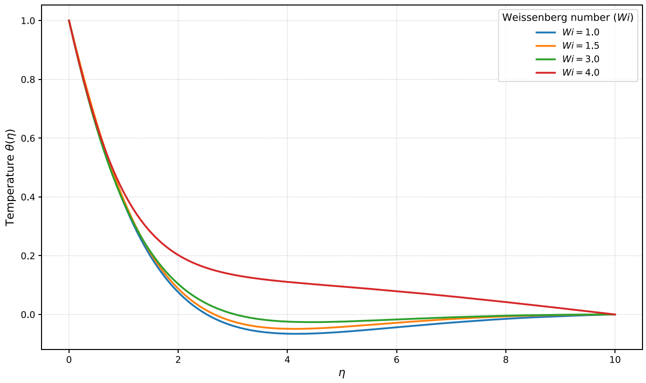

Fig. 26. Profiles of $\theta(\eta)$ for selected values of Wi, showing a progressive rise in $\theta(\eta)$ with increasing elastic effects. The slower thermal decay at larger Wi reflects the additional stretch induced heating encountered in viscoelastic melt flows.

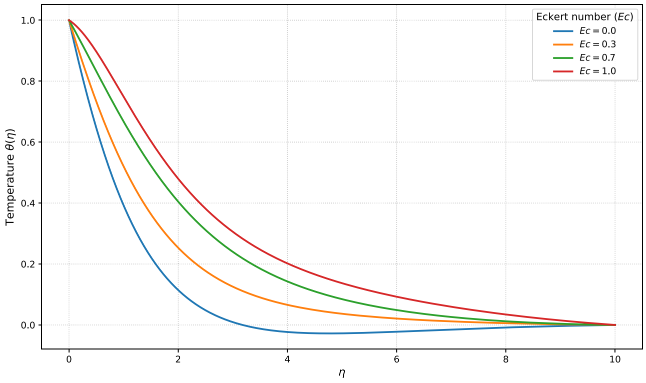

Fig. 27. Profiles of $\theta(\eta)$ for varying Ec, illustrating the strengthening of thermal energy within the layer as dissipation effects grow. Elevated Ec corresponds to greater shear induced heating, a key consideration in high rate polymer melt transport.

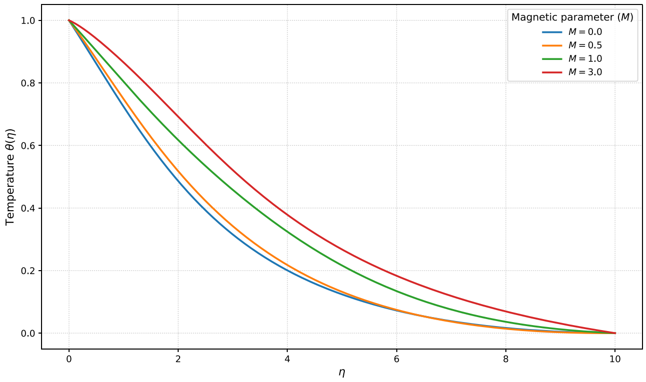

Fig. 28. Profiles of $\theta(\eta)$ for selected values of M, showing higher $\theta(\eta)$ as M increases. The rise at larger M reflects Joule type heating effects that can influence thermal regulation in electrically conducting polymer melts.

the temperature field and supports the reliability of the PINN predictions for subsequent heat transfer analysis in extrusion and coating applications.

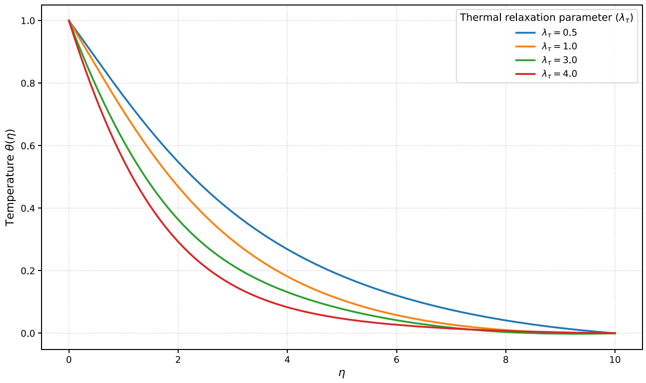

Fig. 29. Profiles of $\theta(\eta)$ for selected values of λ_τ, showing a faster decay of $\theta(\eta)$ as thermal relaxation strengthens. Larger λ_τ suppresses rapid thermal transfer, a feature relevant to delay driven heat propagation in fast moving polymer melts.

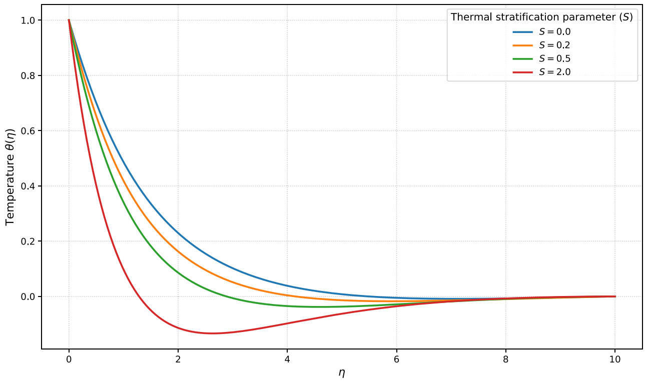

Fig. 30. Profiles of $\theta(\eta)$ for selected values of S, showing a reduction in $\theta(\eta)$ as stratification intensifies. Larger S enhances the upstream thermal gradient, a behavior consistent with layered thermal environments encountered in surface cooling of polymer sheets.

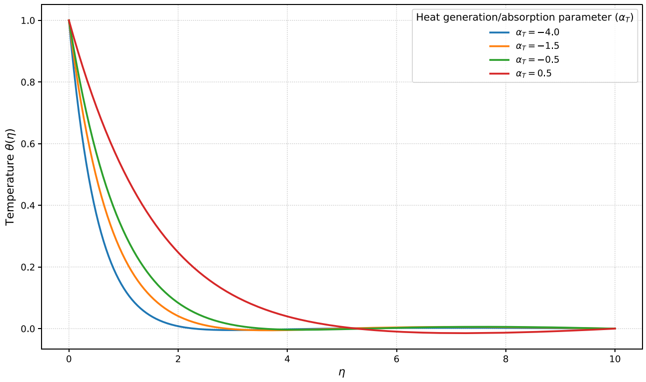

Fig. 31. Profiles of $\theta(\eta)$ for selected values of α_T, showing higher $\theta(\eta)$ under heat generation ($\alpha_T > 0$) and a sharper decay under heat absorption ($\alpha_T < 0$). This sensitivity to α_T reflects the role of internal heat sources in regulating temperature fields within processing melts.

5.3. Concentration behavior

The variation of the dimensionless concentration profile $\phi(\eta)$ is examined under changes in the Schmidt number Sc and the chemical reaction parameter Kr, as shown in Figs. 32–33. The parameters govern mass diffusion strength and reactive depletion within the boundary layer, and their influence is reflected in the rate at which $\phi(\eta)$ decays away from the sheet.

Overall, the concentration profiles decrease smoothly for all parameter values. The sharpest drop appears when either Sc or Kr is large. A higher Sc weakens molecular diffusion, while a higher Kr increases

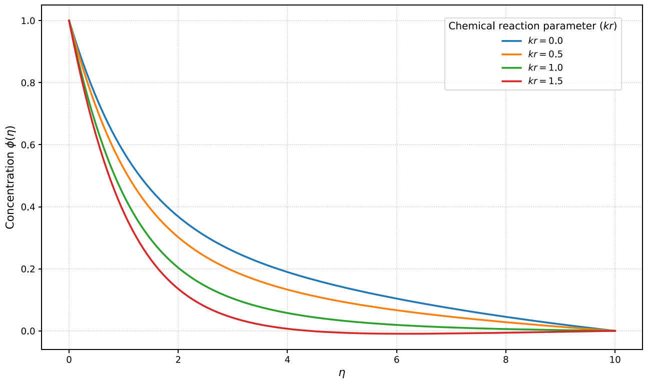

Fig. 32. Profiles of $\phi(\eta)$ for selected values of Kr, showing a faster decay of $\phi(\eta)$ as the reaction rate increases. Larger Kr enhances depletion within the layer, leading to a steeper concentration gradient near the wall.

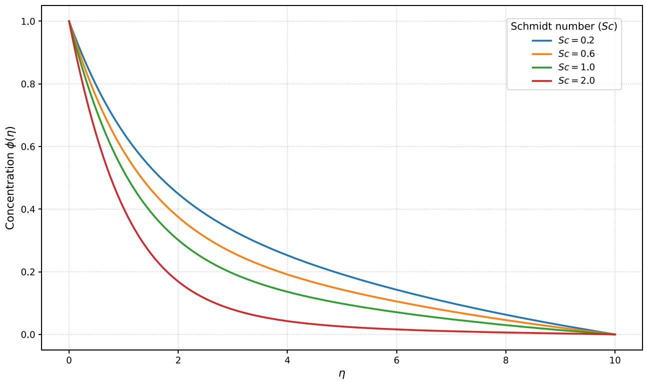

Fig. 33. The profiles of $\phi(\eta)$ indicate a faster decay as Sc increases. Higher Schmidt numbers limit diffusion, which results in a thinner concentration boundary layer.

chemical consumption, so both lead to a stronger mass transfer rate near the wall. These results align with the expected behavior typical of flows, where diffusion and reaction influence third grade viscoelastic fluids.

5.4. Skin-friction and sherwood number analysis

The influence of the controlling parameters on wall shear and mass transfer behavior is illustrated in Figs. 34–35 and summarized in Tables 9–10. Clear and physically consistent trends are observed: parameters related to elasticity and porous resistance enhance $f''(0)$ and the skin-friction coefficient $C_f\sqrt{Re}$, whereas increasing Gr_c or Re reduces the wall shear due to a thinning of the hydrodynamic layer. For mass transfer, both higher Schmidt number and stronger reaction rate lead to steeper gradients at the wall, producing larger Sh_x values. These combined results provide an organized view of how the governing parameters influence near wall transport.

The data in Figs. 34–35 and Tables 9–10 highlight a useful practical feature: wall transport can be tuned by manipulating the underlying physical mechanisms. Enhanced polymer elasticity or reduced porous resistance strengthens the wall shear, while strong buoyancy or high Reynolds numbers suppress it. Conversely, mass transfer is improved when diffusion is limited or when reactive effects are dominant. These findings offer a simple guide for controlling coating, heat treatment and reactive boundary layer applications, where fine adjustment of wall transport parameters is often required.

5.5. Application oriented interpretation for polymer extrusion

The present trends have a natural interpretation for polymer sheet extrusion, where a viscoelastic melt is stretched along a moving surface and transport quantities at the wall determine the quality of the final product. The increase in wall shear with growing elasticity with larger λ and Wi reflects a stronger resistance of the melt against deformation. In a practical setting, this manifests as greater tensile strength of the extruded sheet and reduced surface waviness. Similarly, the rise in $C_f\sqrt{Re}$ with increasing porous resistance P_m reflects the enhanced drag imposed by the resistive substrate, which suppresses near-wall velocity fluctuations and promotes controlled flow development along the die surface, thereby contributing to improved dimensional stability.

Buoyancy driven effects, represented through Gr_T and Gr_C, show the opposite trend: the wall shear decreases when stratification becomes dominant. In polymer processing, these conditions produce thicker thermal or solutal layers that reduce momentum transfer at the surface. This effect is associated with dull regions and non-uniform cooling on the extruded sheet. On the contrary, the increase of the Sherwood number with Sc and Kr indicates stronger mass transport, which is relevant when additives, solvents, or reactive agents are present in the polymer. The results show that adjusting elasticity, porous resistance, and stratification parameters offers a practical means of influencing surface quality, cooling rate, and uniformity during extrusion.

The conceptual arrangement is illustrated in Fig. 36, where the incoming sheet is stretched through a pair of rollers and subsequently cooled. The transition from an unprocessed to a processed sheet reflects the combined influence of deformation and heat removal that governs surface finish in industrial extrusion lines.

Together, the reported inference speed, the mapping between process parameters and model inputs, and the extrusion schematic illustrate how the trained PINN can be embedded as a fast predictive module within an industrial monitoring framework.

6. Conclusions

A hybrid numerical learning framework has been developed to analyze third grade viscoelastic flow with non-Fourier heat conduction over a stretching surface, motivated by thermal regulation in polymer extrusion. Classical solutions obtained using `bvp4c` were reproduced by a Physics Informed Neural Network with pointwise accuracy of order 10^{-3}–10^{-5}, while wall quantities such as $f''(0)$, $C_f\sqrt{Re}$ and Sh_x were captured with the correct magnitude and parametric trends. The results show that elasticity λ, Wi strengthens wall shear, whereas magnetic effect and porous resistance decrease momentum transport. Thermal responses are governed by a balance between dissipation, heat generation, and relaxation effects, with larger Wi, Ec, and α_T thickening the thermal layer, while higher Re and λ_τ promote cooling. Mass transfer is enhanced by increasing Sc and Kr, reflected by larger Sh_x. These findings support the use of viscoelastic and stratification parameters as effective control inputs for regulating surface quality, cooling rate and mass exchange in polymer extrusion and coating systems.

The conclusions drawn in this work are based on a steady, two-dimensional boundary-layer formulation under controlled stretching conditions. While the model captures the dominant near-wall viscoelastic and thermal transport mechanisms relevant to polymer sheet formation, additional effects such as three dimensional flow features, and fully pressure driven die geometries may further influence industrial extrusion processes. Beyond analysis, the trained PINN framework has potential for real time industrial applications. Once trained, the model provides rapid evaluations of flow and thermal quantities for varying operating parameters, making it suitable for online parameter tuning, process monitoring, and control oriented optimization in polymer extrusion. In particular, the mapping between dimensionless inputs and wall transport quantities can be used to adjust the stretching rate,

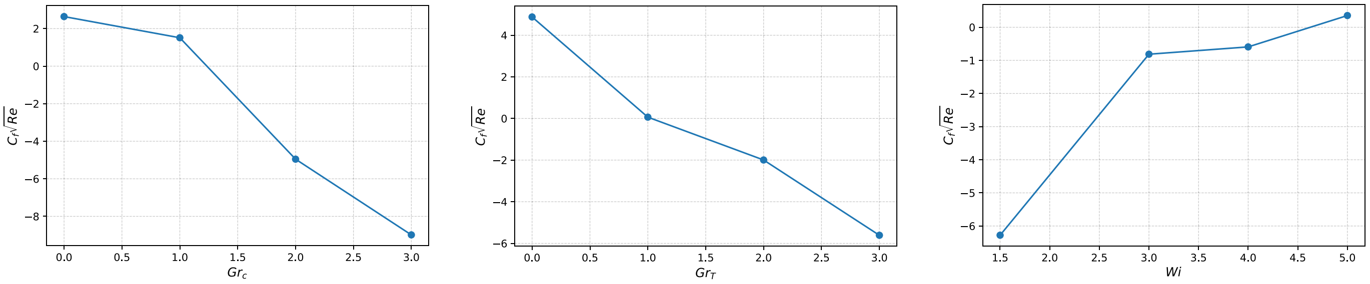

(a) $C_f\sqrt{Re}$ vs Gr_C (b) $C_f\sqrt{Re}$ vs Gr_T (c) $C_f\sqrt{Re}$ vs Wi

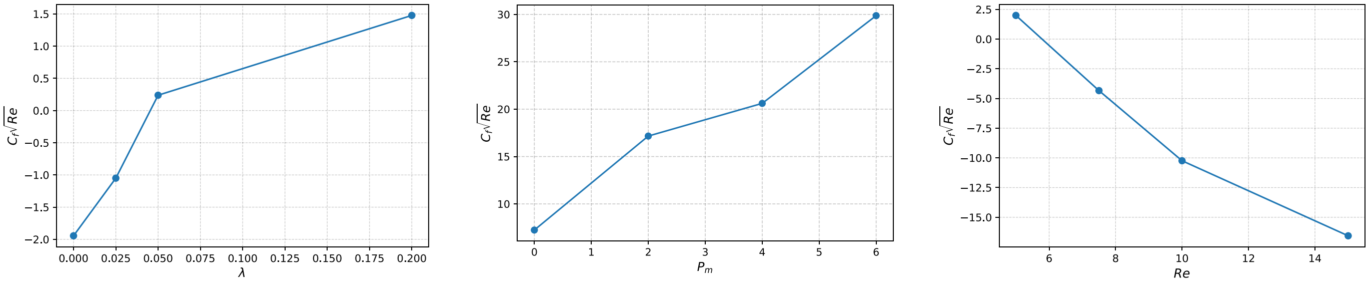

(d) $C_f\sqrt{Re}$ vs λ (e) $C_f\sqrt{Re}$ vs P_m (f) $C_f\sqrt{Re}$ vs Re

Fig. 34. Skin-friction behavior for a range of thermophysical and rheological parameters. Each subfigure shows the variation of the wall shear quantity $C_f\sqrt{Re}$ with respect to a key control parameter.

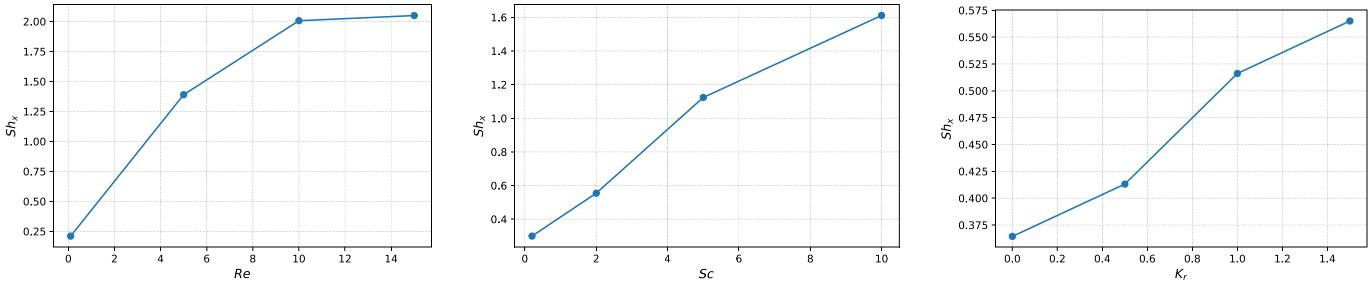

(a) Sh_x vs Re (b) Sh_x vs Sc (c) Sh_x vs Kr

Fig. 35. Sherwood number behavior across key mass transfer parameters. Increasing Re, Sc, and Kr strengthens wall mass transport, reflected in the monotonic rise of Sh_x.

Table 9
Skin-friction quantities $f''(0)$ and $C_f\sqrt{Re}$ for selected control parameters.

(a) $f''(0)$ and $C_f\sqrt{Re}$ vs. P_m.

P_m	$f''(0)$	$C_f\sqrt{Re}$
0.000	$+1.237019 \times 10^{0}$	$+7.241428 \times 10^{0}$
2.000	$+2.528319 \times 10^{0}$	$+17.16053 \times 10^{0}$
4.000	$+2.881140 \times 10^{0}$	$+20.61072 \times 10^{0}$
6.000	$+3.668205 \times 10^{0}$	$+29.87211 \times 10^{0}$

(b) $f''(0)$ and $C_f\sqrt{Re}$ vs. λ.

λ	$f''(0)$	$C_f\sqrt{Re}$
0.000	-4.228149×10^{-1}	-1.944941×10^{0}
0.025	-2.242633×10^{-1}	-1.049726×10^{0}
0.050	$+4.999500 \times 10^{-2}$	$+2.379795 \times 10^{-1}$
0.200	$+2.814004 \times 10^{-1}$	$+1.477394 \times 10^{0}$

(c) $f''(0)$ and $C_f\sqrt{Re}$ vs. Re.

Re	$f''(0)$	$C_f\sqrt{Re}$
5.000	$+1.171311 \times 10^{-1}$	$+1.992580 \times 10^{0}$
7.500	-1.756967×10^{-1}	-4.336788×10^{0}
10.00	-2.728299×10^{-1}	-1.023992×10^{1}
15.00	-2.728299×10^{-1}	-1.656007×10^{1}

(d) $f''(0)$ and $C_f\sqrt{Re}$ vs. Wi.

Wi	$f''(0)$	$C_f\sqrt{Re}$
1.500	-5.799420×10^{-1}	-6.277594×10^{0}
3.000	-4.856657×10^{-2}	-8.139996×10^{-1}
4.000	-2.856857×10^{-2}	-5.930872×10^{-1}
5.000	$+1.428429 \times 10^{-2}$	$+3.536797 \times 10^{-1}$

Table 10
Wall mass transfer quantities for selected Schmidt and reaction parameters.

(a) $\phi'(0)$ and Sh_x vs. Sc.			(b) $\phi'(0)$ and Sh_x vs. Kr.		
Sc	$\phi'(0)$	Sh_x	Kr	$\phi'(0)$	Sh_x
0.200	-4.731786×10^{-1}	$+2.992644 \times 10^{-1}$	0.000	-5.761998×10^{-1}	$+3.644207 \times 10^{-1}$
2.000	-8.765870×10^{-1}	$+5.544023 \times 10^{-1}$	0.500	-6.532256×10^{-1}	$+4.131362 \times 10^{-1}$
5.000	-1.776541×10^{0}	$+1.123583 \times 10^{0}$	1.000	-8.160638×10^{-1}	$+5.161240 \times 10^{-1}$
10.00	-2.547596×10^{0}	$+1.611241 \times 10^{0}$	1.500	-8.933599×10^{-1}	$+5.650104 \times 10^{-1}$

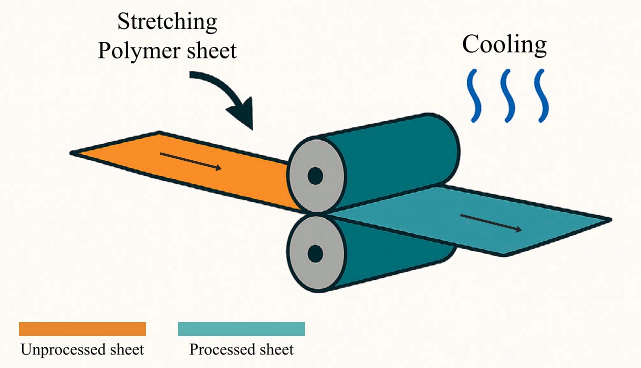

Fig. 36. Schematic of the extrusion process showing the stretching polymer sheet passing through the rollers. The unprocessed sheet is drawn into the rollers, and a cooled processed sheet emerges downstream.

magnetic intensity, or thermal conditions in order to maintain uniform cooling and stable surface quality during operation.

CRediT authorship contribution statement

Syed Hamza Hasnain Kazmi: Formal analysis, Data curation, Conceptualization. **Noor Muhammad:** Writing – review & editing, Writing – original draft, Supervision, Formal analysis. **Taha Aziz:** Writing – review & editing, Visualization, Resources, Project administration. **Haitham M.S. Bahaidarah:** Writing – review & editing, Visualization, Validation, Supervision, Project administration, Methodology.

Declaration of Generative AI and AI-assisted technologies in the writing process

During the preparation of this work the author(s) used ChatGPT (OpenAI) in order to improve the clarity, grammar, and readability of the manuscript. After using this tool, the author(s) reviewed and edited the content as needed and take(s) full responsibility for the content of the publication.

Declaration of competing interest

The authors declare that they have no known competing financial interests or personal relationships that could have appeared to influence the work reported in this paper.

Data availability

No data was used for the research described in the article.

References

[1] B.C. Sakiadis, Boundary-layer behavior on continuous solid surfaces: I. Boundary-layer equations for two-dimensional and axisymmetric flow, AIChE J. 7 (1) (1961) 26–28.
[2] L.J. Crane, Flow past a stretching plate, Z. Angew. Math. Phys. ZAMP 21 (1970) 645–647.
[3] I. Pop, D.B. Ingham, Convective Heat Transfer: Mathematical and Computational Modelling of Viscous Fluids and Porous Media, Elsevier, 2001.
[4] H.I. Andersson, Slip flow past a stretching surface, Acta Mech. 158 (1) (2002) 121–125.
[5] L. Prandtl, Uber flussigkeitsbewegung bei sehr kleiner reibung, in: Verhandl., 3rd Int. Math. Kongr. Heidelberg, Leipzig. (1904), 1905.
[6] R. Cherizol, M. Sain, J. Tjong, Review of non-Newtonian mathematical models for rheological characteristics of viscoelastic composites, Green Sustain. Chem. 5 (01) (2015) 6.
[7] R.S. Rivlin, J.L. Ericksen, Stress-deformation relations for isotropic materials, in: Collected Papers of RS Rivlin: Volume I and II, 1997, pp. 911–1013.
[8] E. Magyari, B. Keller, Exact solutions for self-similar boundary-layer flows induced by permeable stretching walls, Eur. J. Mech. B Fluids 19 (1) (2000) 109–122.
[9] J.B.J. Fourier, Théorie analytique de la chaleur, Gauthier-Villars et fils, 1888.
[10] C. Cattaneo, Sulla Conduzione Del Calore, Vol. 3, Atti Sem. Mat. Fis. Univ. Modena, 1948, pp. 83–101.
[11] C. Cattaneo, Sur une forme de l'equation de la chaleur eliminant la paradoxe d'une propagation instantantee, C. R. 247 (1958) 431–433.
[12] E.R. Smith, P.J. Daivis, B.D. Todd, Measuring heat flux beyond Fourier's law, J. Chem. Phys. 150 (6) (2019).
[13] A.I. Zhmakin, Heat conduction beyond the Fourier law, Tech. Phys. 66 (1) (2021) 1–22.
[14] C.I. Christov, On frame indifferent formulation of the Maxwell–Cattaneo model of finite-speed heat conduction, Mech. Res. Commun. 36 (4) (2009) 481–486.
[15] M. Turkyilmazoglu, Heat transfer enhancement feature of the non-Fourier Cattaneo–Christov heat flux model, J. Heat Transf. 143 (9) (2021) 094501.
[16] J.J. Bissell, Thermal convection in a magnetized conducting fluid with the Cattaneo–Christov heat-flow model, Proc. R. Soc. A 472 (2195) (2016) 20160649.
[17] T. Alboussiere, J.P. Garandet, Buoyancy-driven convection with a uniform magnetic field. Part 1. Asymptotic analysis, J. Fluid Mech. 253 (1993) 545–563.
[18] H. Darcy, Les fontaines publiques de dijon, 1856.
[19] J. Bear, Dynamics of Fluids in Porous Media, Courier Corporation, 2013.
[20] A.M. Megahed, W. Abbas, Non-Newtonian cross fluid flow through a porous medium with regard to the effect of chemical reaction and thermal stratification phenomenon, Case Stud. Therm. Eng. 29 (2022) 101715.
[21] W. Li, S.A. Khan, M. Shafqat, Q. Abbas, T. Muhammad, M. Imran, Computational analysis for efficient thermal transportation of ternary hybrid nanofluid flow across a stretching sheet with Cattaneo-Christov heat flux model, Case Stud. Therm. Eng. 66 (2025) 105706.
[22] K. Hosseinzadeh, M.R. Mardani, M. Paikar, A. Hasibi, T. Tavangar, M. Nimafar, M.B. Shafii, Investigation of second grade viscoelastic non-Newtonian nanofluid flow on the curve stretching surface in presence of MHD, Results Eng. 17 (2023) 100838.
[23] H. Basha, G.J. Reddy, Abhishek, A. Killead, V. Pujari, N.N. Kumar, Numerical modelling of second-grade fluid flow past a stretching sheet, Heat Transf.—Asian Res. 48 (5) (2019) 1595–1621.
[24] F. Hussain, S. Saleem, M. Nazeer, N. Feroz, Q. Shahzad, M.W. Nazir, A note on the multiphase flow of third grade fluid with wall properties, Waves Random Complex Media 35 (3) (2025) 5947–5962.
[25] H.B. Keller, Numerical methods in boundary-layer theory, Annu. Rev. Fluid Mech. 10 (1978) 417–433.
[26] R.D. Russell, L.F. Shampine, A collocation method for boundary value problems, Numer. Math. 19 (1) (1972) 1–28.
[27] M. Raissi, P. Perdikaris, G.E. Karniadakis, Physics-informed neural networks: A deep learning framework for solving forward and inverse problems involving nonlinear partial differential equations, J. Comput. Phys. 378 (2019) 686–707.
[28] I.E. Lagaris, A. Likas, D.I. Fotiadis, Artificial neural networks for solving ordinary and partial differential equations, IEEE Trans. Neural Netw. 9 (5) (1998) 987–1000.
[29] G.E. Karniadakis, I.G. Kevrekidis, L. Lu, P. Perdikaris, S. Wang, L. Yang, Physics-informed machine learning, Nat. Rev. Phys. 3 (6) (2021) 422–440.
[30] S. Cai, Z. Mao, Z. Wang, M. Yin, G.E. Karniadakis, Physics-informed neural networks (PINNs) for fluid mechanics: A review, Acta Mech. Sin. 37 (12) (2021) 1727–1738.
[31] L. Lu, X. Meng, Z. Mao, G.E. Karniadakis, DeepXDE: A deep learning library for solving differential equations, SIAM Rev. 63 (1) (2021) 208–228.

[32] S. Wang, Y. Chen, F. Gong, Y. Fan, B.T. Huang, H. Zhang, Intelligent framework of temperature and humidity field coupling of early-age concrete considering hydration based on physics informed neural network, Int. Commun. Heat Mass Transfer 172 (2026) 110203.

[33] A. Singhal, A.M. Saeed, R. Tiwari, A Chaudhary, Hybrid fractional thermoelastic–machine learning framework for heat and mass transfer in skin tissue: Enhanced simulations using Atangana–Baleanu, Cattaneo–Vernotte models, and KNN–SVM classifiers, Int. Commun. Heat Mass Transfer 171 (2026) 110074.

[34] Z. Mingliang, F.A.M. Al-Yarimi, N. Ijaz, A. Zeeshan, AI-driven entropy optimization in bio-convective third-grade nanofluid flow with electroosmotic effects, Int. Commun. Heat Mass Transfer 172 (2026) 110204.

[35] A. Khan, A. Khan, W. Jamshed, S.M. Hussain, A. Abd-Elmonem, N.S.E. Abdalla, Thermal transport of nonlinear thermal stratification and slip effects in magnetized squeezing nanofluid flow: Applications towards industrial energy efficiency, Int. Commun. Heat Mass Transfer 171 (2026) 110060.

[36] G.E. Karniadakis, I.G. Kevrekidis, L. Lu, P. Perdikaris, S. Wang, L. Yang, Physics-informed machine learning, Nat. Rev. Phys. 3 (6) (2021) 422–440.

[37] Z. Li, H. Zheng, N. Kovachki, D. Jin, H. Chen, B. Liu, A. Anandkumar, Physics-informed neural operator for learning partial differential equations, ACM/IMS J. Data Sci. 1 (3) (2024) 1–27.

[38] A. Michaloglou, I. Papadimitriou, I. Gialampoukidis, S. Vrochidis, I. Kompatsiaris, Physics-informed neural networks in materials modeling and design: a review, Arch. Comput. Methods Eng. (2025) 1–38.

[39] J. Bai, Y. Wang, H. Jeong, S. Chu, Q. Wang, L. Alzubaidi, Y. Gu, Towards the future of physics-and data-guided AI frameworks in computational mechanics, Acta Mech. Sin. 41 (7) (2025) 225340.

[40] S. Tian, Y. Yu, B. Li, A data-driven adaptive deep learning method for nonlinear Schrödinger type equation, Chin. Phys. Lett. 42 (12) (2025) 120001.

[41] S. Tian, B. Li, Z. Zhang, Data-driven ai-and bi-soliton of the cylindrical korteweg–de vries equation via prior-information physics-informed neural networks, Chin. Phys. Lett. 41 (3) (2024) 030201.

[42] P.D. Ariel, Flow of a third grade fluid through a porous flat channel, Internat. J. Engrg. Sci. 41 (11) (2003) 1267–1285.

[43] M. Gahleitner, Melt rheology of polyolefins, Prog. Polym. Sci. 26 (6) (2001) 895–944.

[44] L. Poh, Q. Wu, Y. Chen, E. Narimissa, Characterization of industrial low-density polyethylene: a thermal, dynamic mechanical, and rheological investigation, Rheol. Acta 61 (10) (2022) 701–720.